Gaps in the wall of a perivascular space act as valves to produce a directed flow of cerebrospinal fluid: a hoop-stress model

Yiming Gan, John H. Thomas and Douglas H. Kelley

Department of Mechanical Engineering, University of Rochester, Rochester, NY 14627, USA

YG, 0000-0002-2463-6316; JHT, 0000-0002-7127-8654; DHK, 0000-0001-9658-2954

The flow of cerebrospinal fluid (CSF) along perivascular spaces (PVSs) is an important part of the brain's system for clearing metabolic waste. Astrocyte endfeet bound the PVSs of penetrating arteries, separating them from brain extracellular space. Gaps between astrocyte endfeet might provide a low-resistance pathway for fluid transport across the wall. Recent studies suggest that the astrocyte endfeet function as valves that rectify the CSF flow, producing the net flow observed in pial PVSs by changing the size of the gaps in response to pressure changes. In this study, we quantify this rectification based on three features of the PVSs: the quasi-circular geometry, the deformable endfoot wall, and the pressure oscillation inside. We provide an analytical model, based on the thin-shell hoop-stress approximation, and predict a pumping efficiency of about 0.4, which would contribute significantly to the observed flow. When we add the flow resistance of the extracellular space (ECS) to the model, we find an increased net flow during sleep, due to the known increase in ECS porosity (decreased flow resistance) compared to that in the awake state. We corroborate our analytical model with three-dimensional fluid–solid interaction simulations.

1. Introduction

The flow of cerebrospinal fluid (CSF) along perivascular spaces (PVSs) is an important part of the brain's system for clearing metabolic waste, but the driving mechanisms for this flow are not well understood (see the reviews [1–3]). PVSs surrounding penetrating arteries in the brain cortex are bounded by an outer wall formed by tiled astrocyte endfeet, with gaps between them. These gaps potentially provide a low-resistance pathway for exchange of CSF with interstitial fluid (ISF). Some researchers have suggested that these endfoot gaps might function as one-way valves that drive a net, directed CSF flow by rectifying the flow through the gaps [4,5]. A recent study showed that a net flow through the gaps could be directly related to the net flow in the axial direction in the pial PVSs observed in experiments [5]. In that model, when the pressure in the PVS is greater than the pressure in the extracellular space (ECS), the gaps open and the pressure gradient drives a net flow through the endfoot wall into the ECS. When the pressure in the PVS is less than that in the ECS, the gaps close and the pressure gradient cannot drive as much fluid back into the PVS from the ECS. To compensate, the pressure instead drives an axial flow along the PVS so that the volume of CSF is conserved. This directed flow agrees qualitatively with *in vivo* observations.

Previous studies have shown that if the endfoot gaps are slightly asymmetric, narrower at the interstitial side than at the perivascular side, then the oscillating pressure in the PVS can drive a significant net flow of CSF [4]. Although precise *in vivo* measurements of the shape and dimensions of the endfoot gaps are not yet available, these studies indicate that models of brain fluid flow should explore the possibility that astrocyte endfoot gaps act as valves to convert fluid oscillations into a directed flow. In this study, we show further that an endfoot valve mechanism can exist even without a geometric asymmetry of
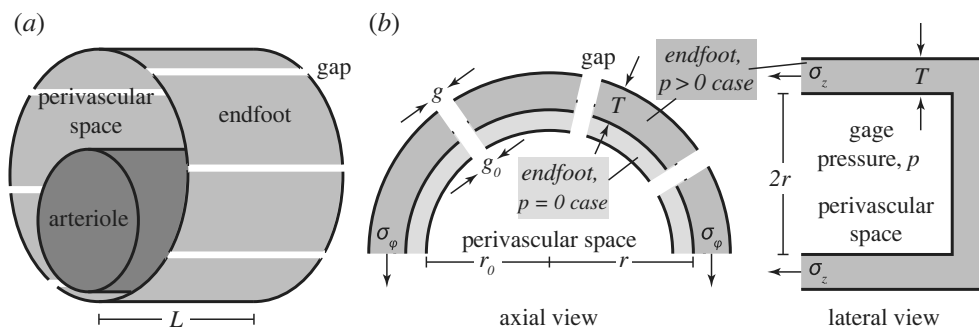
Figure 1. (*a*) A perivascular space lies between an arteriole and the tiled endfeet that form its outer wall, which we idealize as a cylinder of length *L*. (*b*) Pressure in the perivascular space causes the wall radius to expand from r_0 to r, the width of the gaps between endfeet to grow from g_0 to g, and the wall thickness to change from T_0 to T. At equilibrium, forces due to stresses σ_φ and σ_z within the wall must balance forces due to the pressure p on its inner surface.

the gaps. We consider the PVS as an axisymmetric, circular tube encircled by the endfoot wall, assumed to act as a linear elastic solid. Oscillatory pressure in the PVS causes expansion and shrinking of the outer wall. Increased pressure in the PVS causes the outer wall to expand, enlarging the gaps, while decreased pressure shrinks the gaps. As CSF passes through the gaps from the PVS into the surrounding interstitium, this expansion and shrinking acts as a rectifying valve because the fluid flows more easily when the gaps are larger. Here, we present an analytical hoop-stress model [6], using realistic estimates of parameter values to estimate how much expansion and shrinking can be expected, and how effective the rectification would be without any prescribed asymmetry of the gaps. When we include the flow resistance of the ECS in the model, we find an increased net flow during sleep, in agreement with experiments [7,8], due to the known increase in porosity of the ECS (decreased flow resistance) compared to the awake state. We also perform full three-dimensional fluid–solid interaction simulations to corroborate the simpler analytical model and to examine the role of gap geometry.

2. The hoop-stress model

2.1. Description and formulation of the model

We model the PVS as a cylinder of relaxed radius r_0 and length L, as sketched in figure 1. The PVS outer wall is composed of a linear elastic solid having Young's modulus E, Poisson ratio ν and thickness T. The pressure imposed upon the inner surface of the PVS wall by the CSF filling the PVS, measured with respect to the pressure in the surrounding parenchyma, is p. In the equilibrium case, the force due to pressure on the inside surface of the top half of the PVS must be balanced by the force due to azimuthal stress σ_φ in the PVS wall. Assuming the wall is thin ($T \ll r_0$), the stress is approximately uniform within the wall, so $2r_0 p L = 2\sigma_\varphi T L$ (figure 1*b*) and

$$\sigma_\varphi = \frac{pr_0}{T}. \tag{2.1}$$

Similarly, the pressure force on the right half of the PVS must be balanced by the axial stress σ_z in the PVS wall. Again using the thin-wall approximation leads to $p\pi r_0^2 = \sigma_z 2\pi r_0 T$ (figure 1*c*) and

$$\sigma_z = \frac{pr_0}{2T}. \tag{2.2}$$

This expression is valid regardless of the shape of the ends of the PVS; in particular, they need not be flat. However, the ends are assumed to be closed, not open. Finally, the radial stress is $\sigma_r = p$.

Having calculated the stresses, we can determine how much the PVS outer wall and its gaps expand and shrink, that is, determine the strain. According to the Hooke's Law, the azimuthal strain is

$$\epsilon_\varphi = \frac{\sigma_\varphi}{E} - \frac{\nu}{E}(\sigma_z + \sigma_r) = \frac{p}{E}\left(\frac{r_0}{T} - \frac{\nu r_0}{2T} - \nu\right) \approx \frac{pr_0}{ET}\left(1 - \frac{\nu}{2}\right), \tag{2.3}$$

where the rightmost expression arises because $T \ll r_0$ [6]. The radius of the PVS is

$$r = r_0(1 + \epsilon_\varphi). \tag{2.4}$$

As an elastic material expands and constricts, gaps in the material do the same. A gap in the endfoot wall that is oriented in the axial direction thus has width

$$g = g_0(1 + \epsilon_\varphi), \tag{2.5}$$

where g_0 is the gap width when $p = 0$.

Since the total volume of the endfoot wall is constant (for $\nu = 0.5$), we have

$$2\pi r T L = 2\pi r_0 T_0 L, \tag{2.6}$$

where T_0 is the thickness of the endfoot wall when $p = 0$. Combining equations (2.4), (2.5) and (2.6), the thickness can be expressed as

$$T = T_0 \frac{g_0}{g}. \tag{2.7}$$

Knowing how the gap size relates to the strain, and therefore to the pressure, we can determine how the size of the gap affects the flow through it. The volumetric rate at which fluid passes through a wall gap from PVS to parenchyma is

$$Q = \frac{p}{R}, \tag{2.8}$$

where R is the hydraulic resistance of the gap. Neglecting small effects at the ends of the gap, and entrance effects, the hydraulic resistance is that of fully developed Poiseuille flow between infinite parallel flat walls [9,10]:

$$R = \frac{12 \mu T}{g^3 L} = \left(\frac{g_0}{g} \right)^4 R_0, \tag{2.9}$$

where $R_0 = 12 \mu T_0 / g_0^3 L$ is the flow resistance when $p = 0$ and μ is the fluid viscosity. A quantity closely related to the hydraulic resistance and considered in prior studies is the wall permeability k, which is the inverse of the product of the resistance and the surface area of the PVS wall:

$$k = \frac{1}{2 \pi r_0 L R}. \tag{2.10}$$

Combining equations (2.8), (2.9), (2.5) and (2.3) gives

$$Q(t) = \frac{p(t)}{R_0} \left[\frac{p(t) r_0}{ET} \left(1 - \frac{\nu}{2} \right) + 1 \right]^4, \tag{2.11}$$

where the dependence on time t has been written explicitly, for emphasis. We can rewrite equation (2.11) in terms of the strain:

$$Q(t) = Q_0 \epsilon_\varphi (1 + \epsilon_\varphi)^4, \tag{2.12}$$

where $Q_0 = ET R_0^{-1} r_0^{-1} (1 - (\nu/2))^{-1}$ is a constant coefficient, or a characteristic flow rate. For small deformations, $\epsilon_\varphi \ll 1$, we can simplify equation (2.12) by neglecting terms of third and higher order in ϵ_φ, giving

$$Q(t) = Q_0 (\epsilon_\varphi + 4 \epsilon_\varphi^2). \tag{2.13}$$

The first term in equation (2.13) is oscillatory, corresponding to a fluctuating flow of zero mean, and the second term is never negative, corresponding to a net flow.

Having determined how the flow resistance and flow rate depend on pressure, the final step is to determine how well this mechanism would produce net flow if driven by pressure variations that are purely oscillatory. A perfect rectifier, driven with a periodic and zero-mean pressure $p(t)$, would eliminate all fluctuation and produce a steady flow. A more realistic rectifier produces a flow that has both a mean flow and a fluctuating component. For a pressure that fluctuates with fundamental frequency f, the mean flow is

$$\overline{Q} = f \int_{t_0}^{t_0 + f^{-1}} Q(t) \, dt, \tag{2.14}$$

where t_0 is an arbitrary time. The amplitude of the fluctuating component can be defined as

$$Q' = \left(2f \int_{t_0}^{t_0 + f^{-1}} (Q(t) - \overline{Q})^2 \, dt \right)^{1/2}, \tag{2.15}$$

by scaling the root-mean-square amplitude. Then, the effectiveness of rectification can be quantified with the *pumping efficiency* $\eta = \overline{Q}/Q'$, whose value is large when the net, directed flow is large compared to the fluctuations. (The inverse of η was considered in [11] and described as a fluctuation ratio.)

All of the parameters in the model and their assumed numerical values are listed in table 1.

2.2. Results

2.2.1. Binary alternating pressure

As a first example, consider an alternating PVS pressure that is positive and constant for the first half of each cycle and negative and constant for the second half:

$$p(t) = \begin{cases} p_0, & 0 \le t \le \frac{f^{-1}}{2}, \\ -p_0, & \frac{f^{-1}}{2} \le t \le f^{-1}, \end{cases} \tag{2.16}$$

Table 1. Derived quantities.

derived quantities	expression	unit
azimuthal strain ε_φ	$pr_0\,(1-\nu/2)/ET$	
characteristic strain ε_0	$p_0 r_0\,(1-\nu/2)/ET$	
PVS outer radius r	$(1+\varepsilon_\varphi)r_0$	m
endfoot gap width g	$(1+\varepsilon_\varphi)g_0$	m
PVS outer wall thickness T	$T_0/(1+\varepsilon_\varphi)$	m
reference flow resistance R_0	$12\mu T_0/g_0^3 L$	Pa s m^{-3}
flow resistance R	$R_0/(1+4\varepsilon_\varphi)$	Pa s m^{-3}
permeability k	$1/2\pi r_0 LR$	m Pa^{-1} s^{-1}
flow rate $Q(t)$	p/R	m^3 s^{-1}
mean flow rate $\overline{Q}$	$f\int_{t_0}^{t_0+f^{-1}} Q(t)\,\mathrm{d}t$	m^3 s^{-1}
fluctuating rate Q'	$\left(2f\int_{t_0}^{t_0+f^{-1}}(Q(t)-\overline{Q})^2\,\mathrm{d}t\right)^{1/2}$	m^3 s^{-1}
characteristic flow rate Q_0	$ET/R_0 r_0(1-\nu/2)$	m^3 s^{-1}
pumping efficiency η	$\overline{Q}/Q'$	

Table 2. Parameter values.

parameter	value
Young's modulus E	$[10^3\ 5\times10^4]$ Pa
Poisson's ratio ν	0.5
pressure fluctuation amplitude p_0	133 Pa (1 mmHg)
PVS outer radius r_0	15 µm
PVS outer wall thickness T_0	[0.5 µm 2 µm]
viscosity μ	7×10^{-4} Pa s
reference endfoot gap width g_0	20 nm
arteriole length L	1 mm

where $p_0 > 0$ is a constant. The mean volume flow rate is

$$\overline{Q} = 4\frac{p_0}{R_0}\varepsilon_0 = 4Q_0\varepsilon_0^2, \tag{2.17}$$

where $\varepsilon_0 = p_0 r_0(1-\nu/2)E^{-1}\,T^{-1}$ is a characteristic strain. The amplitude of the fluctuating component is

$$Q' = \sqrt{2}Q_0\varepsilon_0, \tag{2.18}$$

and the pumping efficiency is

$$\eta = 2\sqrt{2}\varepsilon_0. \tag{2.19}$$

Now consider the parameter values listed in table 2, which follow Tithof *et al.* [10] and Gan *et al.* [5] and are believed to be reasonably realistic. With these parameter values, the pressure and volume flow rate vary over time as shown in figure 2*a*,*b*. The characteristic strain is $\varepsilon_0 = 0.15$. The pumping efficiency, which depends only on the strain (equation (2.19)), is $\eta = 0.4$ (figure 2*c*). That is, this simple valve mechanism produces a mean volume flow rate about 40% as great as that of the fluctuating flow, when the applied pressure $p(t)$ is purely an alternation.

The characteristic resistance is $R_0 = 2.10 \times 10^{18}$ Pa s m^{-3}. With the alternating pressure, the endfoot gap width g alternates between 23 nm and 17 nm (we used $g_0 = 20$ nm), and the PVS radius r alternates between 17.3 µm and 12.3 µm (we used $r_0 = 15$ µm). The hydraulic resistance R therefore alternates between 8.4×10^{17} Pa s m^{-3} and 3.35×10^{18} Pa s m^{-3}. The mean flow is $\overline{Q} = 3.79 \times 10^{-17}$ m^3 s^{-1}. The amplitude of the fluctuating component is $Q' = 8.96 \times 10^{-17}$ m^3 s^{-1}.

Some of these predictions can be compared directly to prior studies. In one study, neurons in the parenchyma, near the outer wall of a PVS surrounding a penetrating arteriole with diameter approximately 10 µm, were observed to move by approximately 1.5 µm during functional hyperaemia [12]. Another study observed the PVS wall to move by approximately 1 µm, also during functional hyperaemia [8]. A study of natural sleep–wake variation found the PVS wall moving approximately 2 µm [13]. The typical permeability of the PVS wall was estimated to be in the range 2×10^{-11} m Pa^{-1} s^{-1} to 3×10^{-10} m Pa^{-1} s^{-1} [14], based on
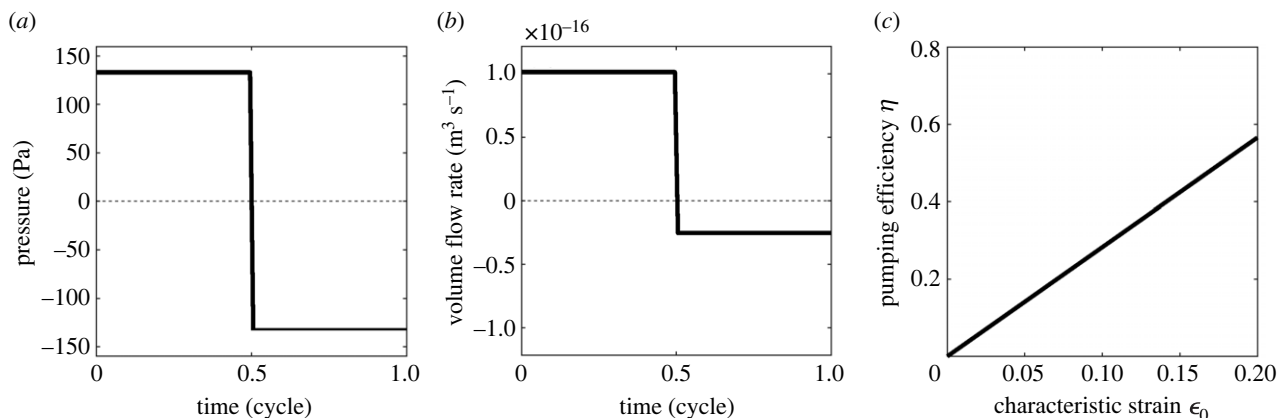
Figure 2. Modelled flow in response to an alternating pressure. With pressure p alternating over time (a), the volume flow rate Q also alternates, but with greater volume flow in the positive direction (from perivascular space to extracellular space) than in reverse (b). The pumping efficiency η increases linearly with increasing characteristic strain ϵ_0 (c).

geometrical factors known from prior electron microscopy [15]. The calculations above use quite different reasoning but result in a similar value of 5.05×10^{-12} m Pa^{-1} s^{-1} using equation (2.10) (Our result is about four times smaller than their lower limit as we only consider a single gap.) With the alternating pressure, the permeability k alternates between 3.72×10^{-12} m Pa^{-1} s^{-1} and 1.10×10^{-11} m Pa^{-1} s^{-1}. Gan *et al.* [5], without elucidating a mechanism in greater detail, modelled pressure-dependent permeability fluctuations as a possible rectification mechanism, finding realistic flows when the permeability was chosen to vary by a factor of 2–5 through each alternation of pressure. The above example of alternating pressure results in permeability varying by a factor of 2.93, within that range. Experimental measurements find $\eta = 2$ [11,16], which implies rectification that is better than predicted in the above example ($\eta = 0.4$) by a factor of five, suggesting that this mechanism could contribute but could not single-handedly achieve the observed rectification.

2.2.2. Sinusoidal alternating pressure

As a second example, we consider PVS pressure varying sinusoidally and having amplitude p_0: $p(t) = p_0 \sin 2\pi f t$. Using equation (2.11) leads to

$$Q(t) = Q_0(4\varepsilon_0^2 \sin^2 2\pi f t + \varepsilon_0 \sin 2\pi f t). \tag{2.20}$$

The mean flow is

$$\overline{Q} = 2Q_0\varepsilon_0^2. \tag{2.21}$$

The amplitude of the fluctuating component is

$$Q' = Q_0\sqrt{\varepsilon_0^2 + 4\varepsilon_0^4}. \tag{2.22}$$

Now it becomes clear that the factor of 2 appearing in equation (2.15) ensures that Q' is the peak amplitude if $p(t)$ varies sinusoidally. The pumping efficiency is

$$\eta = \frac{1}{\sqrt{1 + (1/4\varepsilon_0^2)}}. \tag{2.23}$$

Again using the parameter values listed in table 2, the pressure and volume flow rate vary over time as shown in figure 3a,b. The characteristic resistance and strain remain unchanged. Accordingly, the gap size, PVS radius, resistance and permeability each also vary with the same amplitude as in the previous example, but now sinusoidally. The mean flow is $\overline{Q} = 1.90 \times 10^{-17}$ m^3 s^{-1}. The amplitude of the fluctuating component is $Q' = 6.62 \times 10^{-17}$ m^3 s^{-1}. The pumping efficiency is $\eta = 0.3$. In this case, then, the simple valve mechanism produces a mean flow about one-third as fast as the fluctuating flow, though the applied pressure $p(t)$ is purely a fluctuation. Again, the predicted typical permeability and range of variation of permeability are similar to prior estimates, but the rectification is not as good as observed *in vivo*, suggesting this mechanism could contribute but others may be at play as well.

According to equation (2.23), for sinusoidally varying pressure, as for alternating pressure, the pumping efficiency η depends only on the characteristic strain ε_0. Its variation is shown in figure 3c and is similar to the alternating case.

2.2.3. Asymmetrically alternating pressure

As a third and final example, consider PVS pressure that varies asymmetrically in time, rising more rapidly than it decays, a characteristic that has been proposed to aid in rectification [12]. One simple asymmetric waveform, similar to one proposed
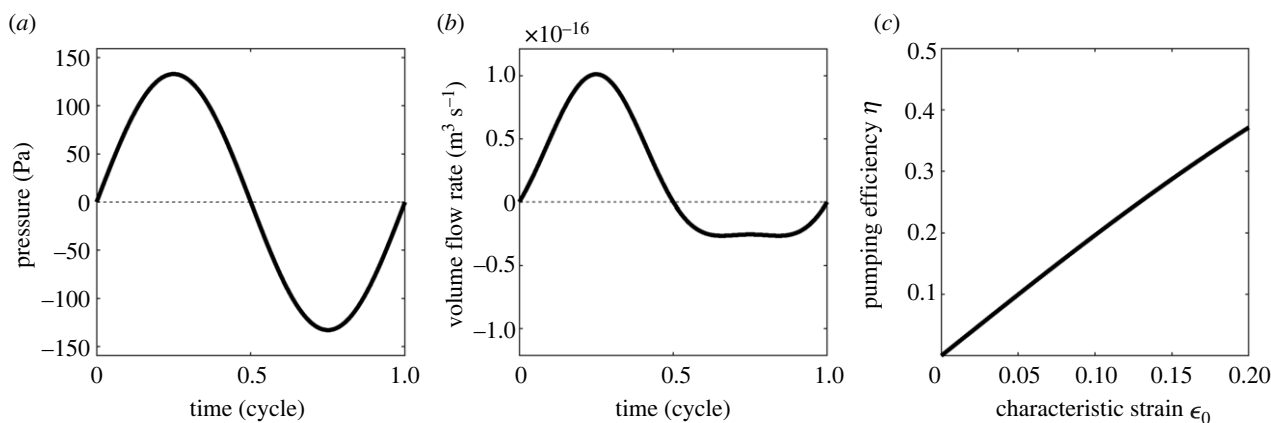
Figure 3. Modelled flow in response to a sinusoidal pressure variation. With pressure p varying sinusoidally with time (a), the volume flow rate Q also varies, but with greater volume flow in the positive direction (from perivascular space to extracellular space) than in the reverse direction (b). The pumping efficiency η increases monotonically with increasing characteristic strain ϵ_0 (c).
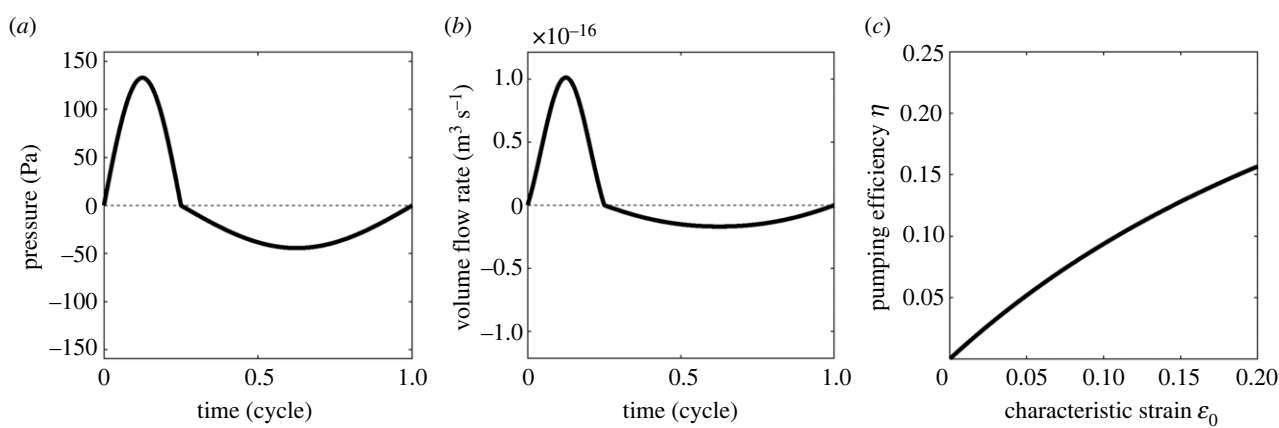

Figure 4. Modelled flow in response to an asymmetric pressure variation. With brief, high positive pressure followed by longer-lived, gentler negative pressure (a), the volume flow rate Q also varies, but with greater volume flow in the positive direction (from perivascular space to extracellular space) than in the reverse direction (b). The pumping efficiency η increases monotonically with increasing characteristic strain ε_0 (c).

previously [5] is

$$p(t) = \begin{cases} p_0 \sin(4\pi f t), & 0 \le t < \frac{f^{-1}}{4} \\ \frac{p_0}{3} \sin\left(\frac{4}{3}\pi f(t - f^{-1})\right), & \frac{f^{-1}}{4} \le t < f^{-1}. \end{cases} \tag{2.24}$$

The volume flow rate is

$$Q(t) = \begin{cases} Q_0(\varepsilon_0 \sin(4\pi f t) + 4\varepsilon_0^2 \sin(4\pi f t)^2), & 0 \le t < \frac{f^{-1}}{4} \\ Q_0\left(\frac{1}{3}\varepsilon_0 \sin\left(\frac{4}{3}\pi f(t - f^{-1})\right) + \frac{4}{9}\varepsilon_0^2 \sin\left(\frac{4}{3}\pi f(t - f^{-1})\right)^2\right), & \frac{f^{-1}}{4} \le t < f^{-1}. \end{cases} \tag{2.25}$$

The mean flow is

$$\overline{Q} = Q_0\left(\frac{2}{3}\varepsilon_0^2\right). \tag{2.26}$$

In this case, the fluctuating flow rate is in a more complicated analytical form. Here, we show only the numerical solution. The amplitudes of the fluctuating component and the pumping efficiency are calculated numerically (figure 4). The pumping efficiency reaches 0.15 in the range of strains considered, putting it in the same order of magnitude as in the two earlier examples, though slightly less. At least with the mechanism considered here, this asymmetric pressure profile does not produce superior rectification.

2.2.4. Flow resistance in the extracellular space and wake/sleep variations

If fluid passes from the PVS to the ECS through valve-like endfoot gaps, then the pumping efficiency of the system will depend, in part, on the hydraulic resistance of the ECS. An oscillatory pressure variation will also drive a pressure response in the ECS. To model these phenomena, we consider the case in which the ECS has a non-zero but constant resistance and the pressure is allowed
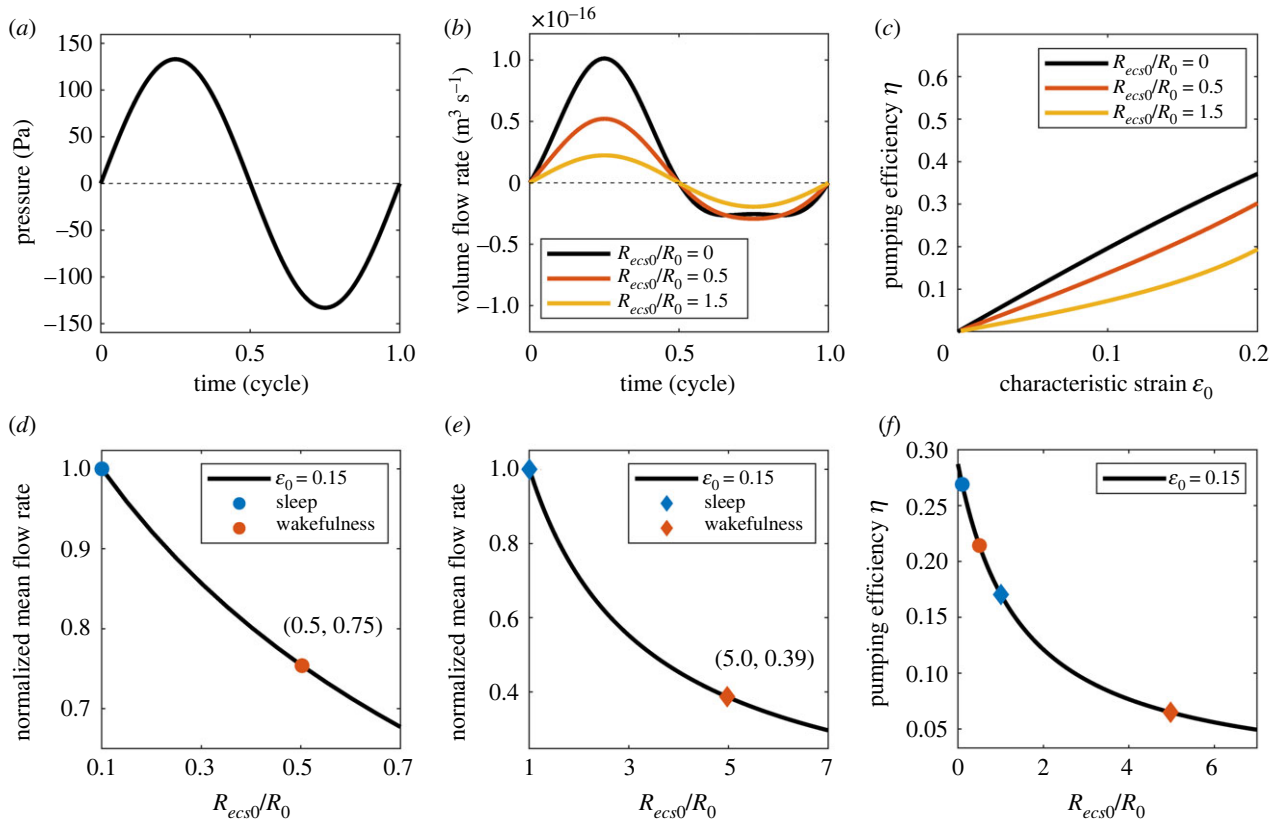
Figure 5. (a) Modelled flow in response to a sinusoidal pressure variation, accounting for resistance in the extracellular space (R_{ecs0}). (b) Increasing R_{ecs0}/R_0 reduces the amount by which forward flow exceeds reverse flow. (c) Increasing R_{ecs0}/R_0 reduces the rate of increase of pumping efficiency with increasing characteristic strain. (d) For the case where $R_{ecs0}/R_0 = 0.1$ during sleep, the mean flow rate during wakefulness (the red dot, $R_{ecs0}/R_0 = 0.5$) is 75% of the mean flow rate during sleep (the blue dot). In the regime $R_{ecs0}/R_0 < 1$, increasing R_{ecs0}/R_0 decreases the normalized mean volume flow rate. (e) For the case where $R_{ecs0}/R_0 = 1$ during sleep, the mean flow rate during wakefulness (the red diamond, $R_{ecs0}/R_0 = 5$) is 39% of the mean flow rate during sleep (the blue diamond). In the regime $R_{ecs0}/R_0 \geq 1$, increasing R_{ecs0}/R_0 decreases the normalized mean volume flow rate. (f) For both regimes, $R_{ecs0}/R_0 < 1$ and $R_{ecs0}/R_0 \geq 1$, the pumping efficiency decreases monotonically with increasing R_{ecs0}/R_0. The pumping efficiency is smaller during wakefulness than during sleep for the cases considered in (d,e) (the dots and the diamonds).

to vary across the ECS but held constant at the outer boundary (which models the PVS of the nearest vein). Equation (2.8) is then replaced by

$$Q = \frac{p}{R + R_{ecs0}}, \tag{2.27}$$

where R_{ecs0} is the flow resistance of the ECS between the outer wall of the arterial PVS and the outer boundary. According to equation (2.12), the total flow resistance can be written as

$$R + R_{ecs0} = R_0\left[\left(\frac{g_0}{g}\right)^4 + \frac{R_{ecs0}}{R_0}\right]. \tag{2.28}$$

The pressure drop across the endfoot wall is then

$$p' = \frac{R_0}{R_0 + R_{ecs0}}p(t). \tag{2.29}$$

This pressure drop causes an azimuthal strain, which can be rewritten as

$$\varepsilon_\varphi = \frac{(R_0/(R_0 + R_{ecs0}))p(t)r_0}{ET}\left(1 - \frac{\nu}{2}\right). \tag{2.30}$$

Combining equations (2.27), (2.29) and (2.28) gives the following expression for the total flow rate:

$$Q(t) = \frac{p(t)((R_0/(R_0 + R_{ecs0}))(p(t)r_0/ET)(1 - (\nu/2)) + 1)^4}{R_0(1 + ((R_0/(R_0 + R_{ecs0}))(p(t)r_0/ET)(1 - (\nu/2)) + 1)^4(R_{ecs0}/R_0))}. \tag{2.31}$$

Again, we can rewrite equation (2.31) in terms of ε_φ and neglect terms of third and higher order in ε_φ, giving

$$Q(t) = Q_0\frac{(\epsilon_\varphi + 4\epsilon_\varphi^2)}{1 + 4\epsilon_\varphi(R_{ecs0}/(R_0 + R_{ecs0}))}. \tag{2.32}$$

The denominator in this expression describes an improved estimate of flow rate, taking into account the flow resistance of the ECS. For this model, we consider the same sinusoidal pressure waveform as before (figure 5a). For different values of R_{ecs0}/R_0, we still

observe a greater volume flow in the positive direction than in the reverse direction, and a pumping efficiency that increases monotonically with increasing characteristic strain (figure 5b,c). However, as R_{ecs0}/R_0 increases, the net flow volume and the pumping efficiency decrease (figure 5b–f). If the flow resistance of the ECS is much smaller than the flow resistance of the endfoot wall ($R_{ecs0}/R_0 \ll 1$), the model is equivalent to that in the previous model, where the pressure in the ECS is considered to be constant (the black lines in figure 5b,c). If the flow resistance of the ECS is much larger than the flow resistance of the endfoot wall ($R_{ecs0}/R_0 \gg 1$), the pumping efficiency is small and the valve mechanism is ineffective (figure 5f).

Less CSF flow is observed during wakefulness than during sleep. The permeability of the ECS decreases by about a factor of five during wakefulness compared to sleep [7,10,17,18]. Hence, the flow resistance of the ECS, which is inversely proportional to the permeability (equation (2.10)), is about five times larger during wakefulness than during sleep. We can apply our present model to compare the performance of the valve mechanism during wakefulness to its performance during sleep. We consider two representative values of R_{ecs0}/R_0 during sleep, $R_{ecs0}/R_0 = 0.1$ (figure 5d) and $R_{ecs0}/R_0 = 1$ (figure 5e), and in each case the value of R_{ecs0}/R_0 is five times greater during wakefulness. For these two cases, we find that the mean flow rate during wakefulness is either 75% or 39% of the flow rate during sleep, for the same value of ε_0. Note that for the case of $R_{ecs0}/R_0 = 1$, a threefold larger pressure in the PVS is needed to cause the same characteristic strain (ε_0) during wakefulness, according to equation (2.30). The pumping efficiency decreases monotonically as R_{ecs0}/R_0 increases (figure 5f), and, hence, is always smaller during wakefulness than during sleep.

We can estimate the possible range of values of R_{ecs0}/R_0 from previous studies. The flow resistance of the ECS derived by Holter et al. [19] (see also [10]) is

$$R_{ecs0} = \frac{\mu \ln \left(\left[(1 - (l_{a-v}/r_{artery}))\right]^2 \right)}{2\pi k_{ecs} l}, \tag{2.33}$$

where $l_{a-v} \approx 200\,\mu m$ is the median distance between an artery and the nearest venule, $r_{artery} \approx 8\,\mu m$ is the radius of the artery and k_{ecs} is the permeability of the ECS, which falls in the range from $1.2 \times 10^{-17}\,m^2$ [19] to $4.5 \times 10^{-15}\,m^2$ [20] . Therefore, R_{ecs0} is in the range from $3.5 \times 10^{16}\,Pa\,s\,m^{-3}$ to $1.6 \times 10^{14}\,Pa\,s\,m^{-3}$. A previous study estimates the endfoot permeability in the range $2 \times 10^{-11}\,m\,Pa^{-1}\,s^{-1}$ to $3 \times 10^{-10}\,m\,Pa^{-1}\,s^{-1}$ [14]. According to equation (2.10), which relates the permeability and the flow resistance, the endfoot flow resistance R_0 is in the range $3.5 \times 10^{16}\,Pa\,s\,m^{-3}$ to $5.3 \times 10^{17}\,Pa\,s\,m^{-3}$. Combining the ranges of both parameters, R_{ecs0}/R_0 falls in the range 2.8×10^{-4} to 1. If $R_{ecs0}/R_0 \ll 1$, the ECS resistance is negligible and the model is equivalent to the previous model. Therefore, the two cases $R_{ecs0}/R_0 = 0.1$ and 1 during sleep (figure 5d–f) should adequately supplement the previous model.

3. The three-dimensional computational model

In order to corroborate the findings of our analytical hoop-stress model, we created a corresponding three-dimensional (3D) computational model of the fluid–solid interactions involved in the flow rectification (figure 6). The model employs the software packages preCICE, OpenFOAM and Fenics [21–25]. The preCICE package is used for the partitioned fluid–structure interaction, coupling OpenFOAM, the fluid-domain solver, and Fenics, the solid-domain solver. OpenFOAM solves for the laminar flow with a moving mesh, and Fenics solves the solid mechanics of the wall using a finite-element method. A segment of the PVS with a length of 30 μm is considered. The endfoot wall, immersed in the computational mesh, separates the outer ECS (at radius 25 μm) from the inner PVS (at radius 15 μm) (figure 6a,d). The endfoot gaps are modelled as two square holes of side length 2 μm in the endfoot wall (figure 6a–d; only one hole is shown, and the other is placed symmetrically, on the back of the PVS). The thickness of the endfoot wall is 2 μm. The elastic modulus of the endfoot wall is 30 kPa, and the Poisson ratio is 0.49. The density of the endfoot wall (solid phase) is 100 kg m^{-3}. The CSF density is 1000 kg m^{-3}, and the dynamic viscosity of the CSF is 10^{-3} Pa s.

In figure 6c, a positive pressure ($p = 100$ Pa) is applied to both end boundaries of the PVS, where the ends of the endfoot wall are clamped. Positive pressure in the PVS causes a dilation of the endfoot wall and the gaps, pushing CSF from the PVS into the ECS. In figure 6e, a negative pressure ($p = -100$ Pa) is applied to both end boundaries of the PVS, causing constriction of the endfoot wall and the gaps while pulling CSF from the ECS into the PVS. We vary the pressure and measure the maximum azimuthal strain by calculating the maximum radial strain $\epsilon = r/r_0 - 1$ from the simulations (according to equation (2.4)), and we get results similar to those in the hoop-stress model, as shown in figure 6c. In figure 6f, we calculate the pumping efficiency η using the steady-state solutions from each group of simulations with pressure of the same amplitude but the opposite sign, and compare it with the binary alternating hoop-stress model in figure 3c. We find that the results compare favourably. The 3D simulations thus corroborate the hoop-stress model and the basic flow rectification mechanism. In figure 6g,h, we show how the slit-shaped gaps (1 μm × 4 μm) deform under the same conditions considered for square holes. Compared to the square cases (figure 6c,d), we observe a more dramatic change in gap size due to bending in addition to uniform stretching, and therefore a higher pumping efficiency (figure 6i).

The slit shape is a better model of the realistic geometry of the gaps, which are long and narrow, so the pumping efficiency could be higher than that predicted by the hoop-stress model (figure 6f). However, gaps do not always align with the PVS axis. In figure 7, we compare the case where the gaps are placed axially (figure 7a) and the case where the gaps are placed perpendicular to the axis (figure 7b). With the same pressure applied ($p = -100$ Pa), we find that the perpendicular gaps (figure 7b) deform less than the axial gaps (figure 7a). That observation is consistent with the fact that simulations of perpendicular gaps more closely match our analytical model (figure 7c), which does not account for the extra deformation.

The numerical set-up was tested using two meshes of different size to ensure that the spatial resolution is sufficient. In figure 8a, we use the cases of $p = 1$ Pa and $p = 10$ Pa and calculate the maximum strain and the pumping efficiency, finding good agreement between the meshes. We compute the steady-state result upon convergence, with a relative error less than
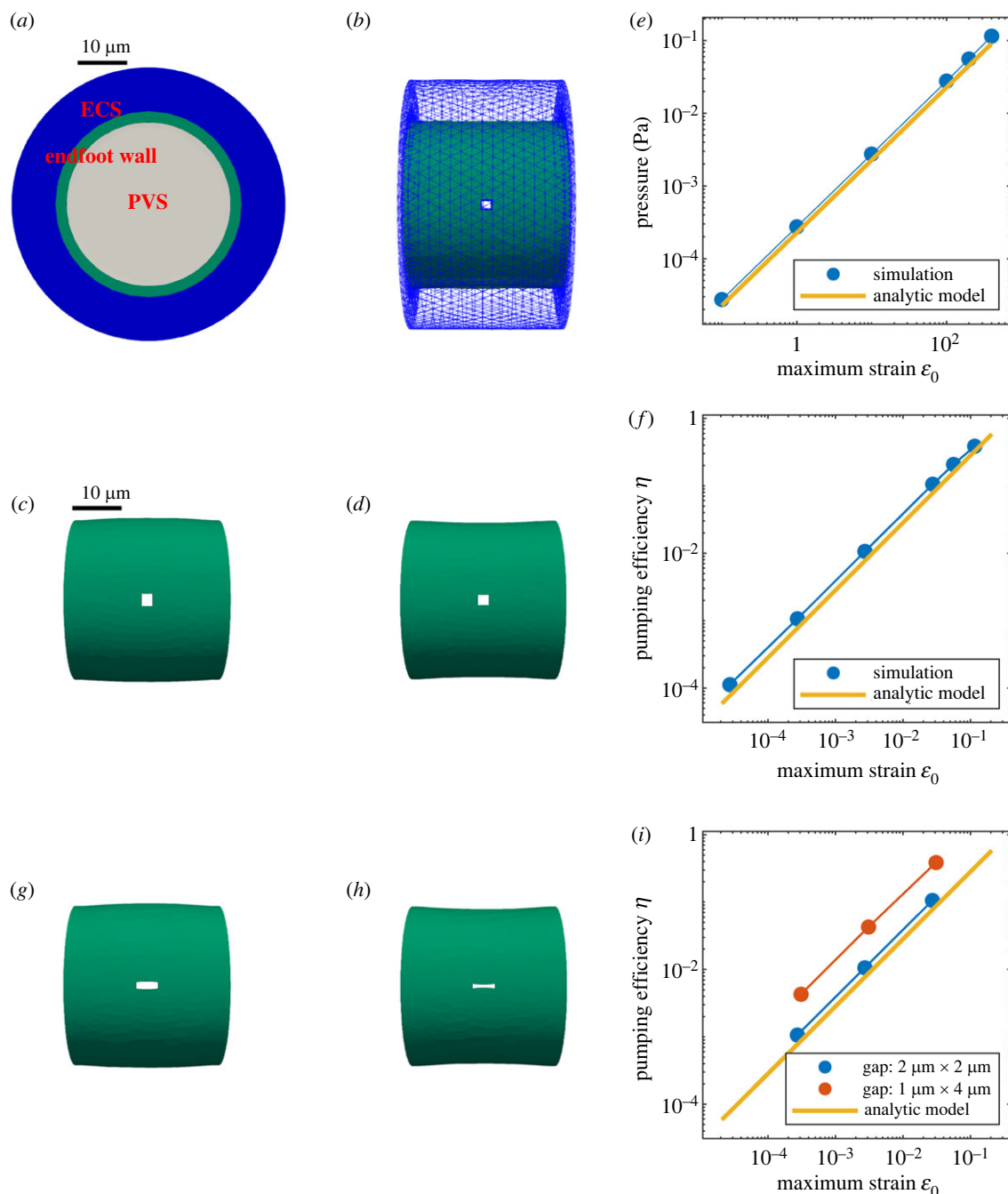
Figure 6. (a) Axial view of the numerical model of a segment of the perivascular space. The solid endfoot wall is immersed in the fluid domain, separating the outer extracellular space (ECS, radius 25 μm) from the inner perivascular space (PVS, radius 15 μm). The axial length of the tube is 30 μm. (b) Lateral view of the numerical model. The blue wire frame shows part of the internal mesh for the fluid domain. The endfoot gaps are modelled as two square holes (width 2 μm) on the endfoot wall surface. The thickness of the endfoot wall is 2 μm. (c) A positive pressure boundary condition ($p = 100$ Pa) applied to both ends of the PVS causes a dilation of the endfoot wall and the gaps in it. (d) A negative pressure boundary condition ($p = -100$ Pa) applied to both ends of the PVS causes a constriction of the endfoot wall and the gaps in it. (e) Strain varies similarly with pressure in simulations and in the analytical hoop-stress prediction. (f) Pumping efficiency varies similarly with strain in the simulations and in the analytical hoop-stress prediction. (g) For the slit-shaped gaps, positive pressure ($p = 100$ Pa) causes nonuniform deformation and more expansion of the gaps compared to the square gaps in (c). (h) For the slit-shaped gaps, negative pressure ($p = -100$ Pa) causes more shrinkage of the gaps compared to the square gaps in (d). (i) Strain varies similarly with pressure in simulations and in the analytical hoop-stress prediction. We observed higher pumping efficiency in the slit-shaped gaps compared to the square gaps, indicating the stronger rectification due to the extra, uneven deformation. Simulations with pressure amplitudes of $p_0 = [1, 10, 100]$ Pa are plotted.

0.001 (figure 8b). The length of the tube does not appear in the expression for the pumping efficiency in the hoop-stress model, which essentially assumes a PVS of infinite length. In figure 8c, we compare simulations with different finite tube lengths (30 μm, 60 μm, 90 μm) but the same slit-shape gap (1 μm × 4 μm), and find that the maximum stress and pumping efficiency do not differ appreciably with tube length over this range of values. For longer tubes, the gaps are farther away from the clamped ends. The observation of higher pumping efficiency due to extra deformation is consistent across different tube lengths. We can therefore confirm that the extra deformation is not an effect of the clamped boundaries at the ends of the tube, but instead is an effect of the aspect ratio of the gaps.
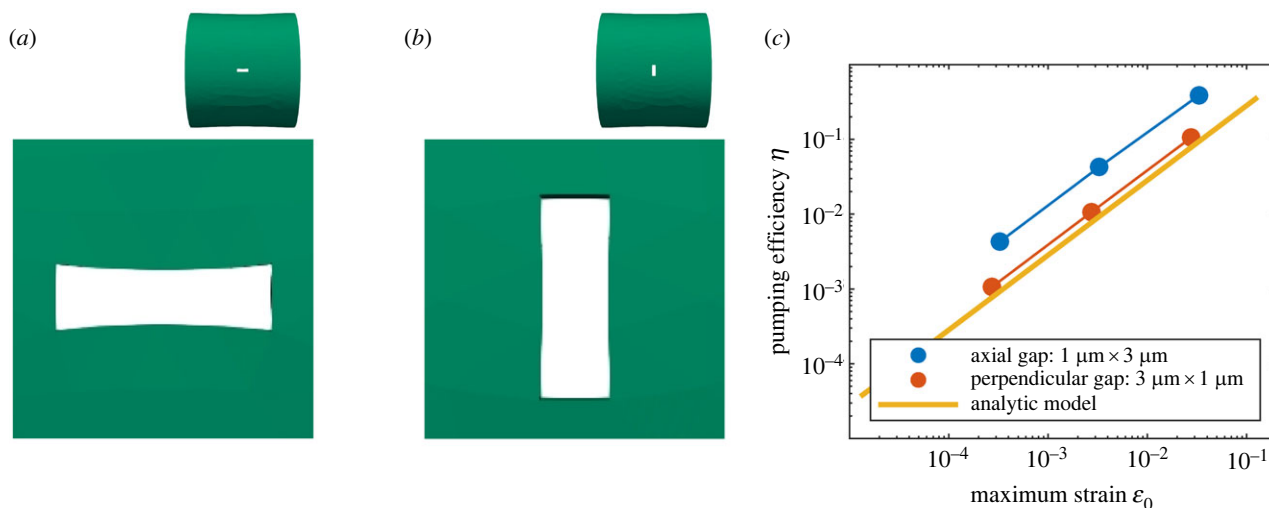
Figure 7. (a) The constriction of a slit-shaped gap (1 μm × 3 μm), aligned with the PVS axis, when negative pressure ($p = -100$ Pa) is applied to both ends of the PVS. (b) The constriction of a slit-shaped gap (3 μm × 1 μm), perpendicular to the PVS axis, when negative pressure ($p = -100$ Pa) is applied to both ends of the PVS. An axial slit constricts and deforms more. In each case, the lower image is an enlargement of the upper image. (c) Strain varies similarly with pressure in simulations and in the analytical hoop-stress prediction, and agreement is closer for slits perpendicular to the PVS axis. Simulations with pressure amplitudes of $p_0 = [1, 10, 100]$ Pa are plotted.
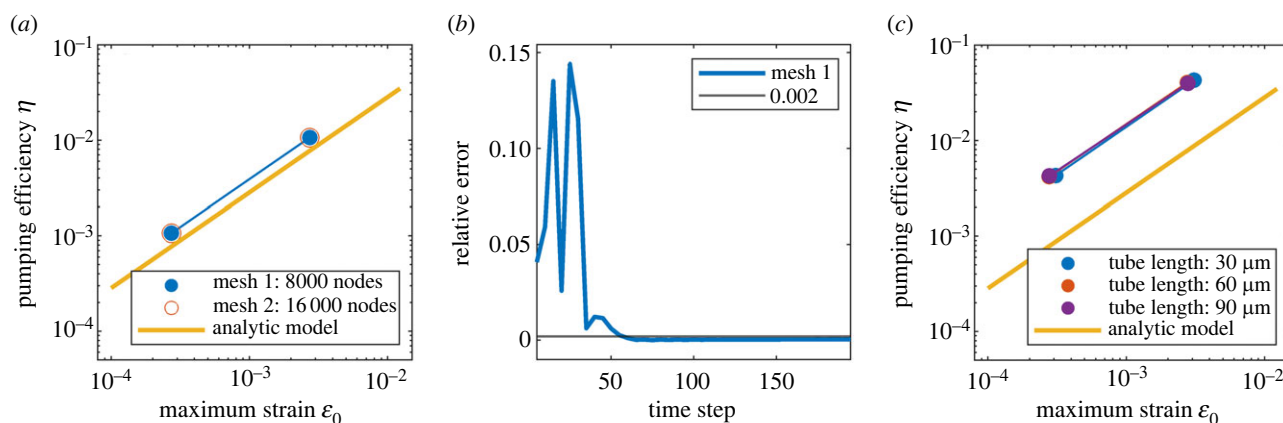

Figure 8. (a) Computational meshes with 8000 or 16 000 nodes lead to nearly identical predictions of pumping efficiency, in simulations of alternating pressure ($[-1, 1]$ Pa and $[-10, 10]$ Pa). The gap size was 2 μm × 2 μm. (b) Upon convergence after 200 time steps ($dt = 0.0005$ s), the relative error between the adjacent steps is smaller than 0.001 for the 8000-node mesh. (c) Varying the tube length (domain size) had little effect on pumping efficiency. The gap was a 1 μm × 4 μm slit, aligned axially.

4. Discussion

Here, we provided a model of a PVS, with a simple annular configuration, in which the endfoot gaps in the outer wall rectify the oscillatory flow of CSF to produce a directed flow, in the absence of any geometric asymmetry of the gaps. Our model is based on reasonable values of several parameters of the glymphatic system, taken from published sources, though some are highly variable or have large uncertainties. The key quantity is the stretching of the endfoot wall. Experiments have shown that neurovascular-coupled artery motion drives an endfoot wall deformation of ≈1.5 μm for a penetrating artery PVS with a radius of ≈10 μm [12,13]. We can therefore estimate an azimuthal strain of $\varepsilon \approx 0.15$, from which our model predicts a pumping efficiency of ≈0.4 for the case of binary alternating pressure, or ≈0.3 for the case of sinusoidally varying pressure. In other words, this simple valve mechanism produces a mean flow about 30% to 40% as fast as the oscillatory flow, even though the pressure variation is a purely symmetric alternation.

We considered the effects of ECS resistance, which connects in series with the flow resistance of the endfoot wall. Including ECS resistance suppresses the valve mechanism, but as long as the resistance of the ECS does not exceed that of the endfoot wall by more than an order of magnitude, it does not greatly change the results. That range of ECS resistances is reasonable, according to prior publications. The astrocyte endfoot wall is two orders of magnitude less permeable than a similarly thick layer of ECS [14], whereas the ECS is two orders of magnitude thicker than the endfoot wall in our model (we consider the distance between the arterial PVS and the nearest venule, an efflux path in the glymphatic model, taking that distance to be 200 μm, following [19]). Therefore, it is likely that the ECS and endfoot wall have resistances of similar magnitude. However, values of both of these parameters have large uncertainty and require more precise measurements.

During wakefulness, when the resistance of the ECS increases fivefold, our model predicts significantly less net flow (61% less for $R_{ecs0}/R_0 = 1$ if ε_0 is left unchanged; see figure 5e) and lower pumping efficiency. These predictions are consistent with *in vivo*

observations, which find little net CSF flow in PVSs during wakefulness [7]. Note that three times as much pressure is needed to cause the same characteristic strain ε_0 during wakefulness as during sleep, according to our model.

An equation that relates the deformation and the axial flow resistance has been used in previous work [26,27]. Our model expresses how the deformation changes the radial flow resistance based on the simplified, linear hoop-stress relation and corroborates this dependence with 3D numerical simulations. The model assumes linear elastic behaviour of the endfoot wall, based on experimental observations of small deformations (less than 20%): for larger deformations, nonlinearity should be considered for better accuracy. Future experiments are needed in order to validate various aspects of the model.

The extent to which the deformation changes the flow resistance of a layer of poroelastic tissue (the endfoot wall, in this case) depends on several factors, none of which are known to high accuracy. Future experiments reducing the uncertainty in the size of the gaps between endfeet, the thickness of the endfeet, their material properties E and v, and the pressure fluctuations in PVSs would make models like ours more precise. Many features of the endfoot geometry are too small to be resolved *in vivo* but are likely to be altered during the fixation processes necessary for postmortem electron microscopy, so inference from system dynamics may be necessary. Similarly, the pressure can be estimated from observed stretching if the material properties are well known. The magnitude of endfoot wall stretching due to cardiac pulsation is also highly uncertain, though it seems to be smaller than current *in vivo* imaging can resolve. On the other hand, functional hyperaemia deforms endfoot walls by about 1 μm *in vivo* [8,12].

With realistic pressure pulsation amplitudes, for either functional hyperaemia or cardiac pulsation, our model predicts pumping efficiency four to five times smaller than what is measured *in vivo* (figures 2–4). Therefore, the rectification mechanism presented here is not sufficient to explain the observed CSF flow by itself. That said, this mechanism might work in concert with others, such as bending-based mechanisms [4] or impedance pumping [8]. Modelling the flow that occurs when valve mechanisms are combined is a fruitful topic for future work.

Astrocyte endfeet are densely decorated with the water channel protein aquaporin-4 (AQP4). Knocking out that protein or preventing its preferential expression on the endfeet hinders glymphatic function [28], but the fluid dynamical mechanism by which AQP4 enables flow is not precisely known. If AQP4 allows substantial movement of water in and out of endfeet as they stretch under pressure, it might thin the endfoot wall and widen the endfoot gaps when pressure in the PVS is high, thereby increasing the pumping efficiency. Future work could test this speculation by simulating endfeet as a poroelastic material instead of a linear solid, using an approach similar to that of Romanò *et al.* [29].

The mechanism we have considered always favours an outward radial flow, because high pressure in the PVS simultaneously expands the gaps in the endfoot wall and pushes CSF outward through those gaps. Fluid is known to flow outward from arterial PVSs. It is believed, however, that in venous PVSs or nerve sheaths, fluid flows inward through their walls on its way out of the brain. Our mechanism would not favour that inward radial flow, but also would do little to oppose it, because veins and nerves do not pulse appreciably. This sort of valve action, then, would be limited to arterial PVSs.

In the model of sinusoidal alternating pressure, which involves dynamical wall motions, the wall velocity is neglected for simplicity. When the wall is moving, the velocity driven by the pressure difference across the wall is actually the fluid velocity relative to the wall velocity, yet the model remains valid. In experiments, the wall velocity due to cardiac pulsation is ≈10 μm s^{-1}, and that due to slow neurovascular coupling is ≈1 μm s^{-1}. The CSF flow velocity relative to the endfoot wall (which represents the net flow transport) is expected to be less than ≈1 μm s^{-1} [19]. Since the wall velocity could be an order of magnitude greater than the CSF relative velocity, it would be difficult to measure the latter.

In our 3D simulation, we model the gaps as two holes in the endfoot wall, with a hole width of ≈2 μm. In reality, there are numerous gaps along the endfoot wall, and the gap width *in vivo* could be as small as 20 nm, while the radius of the wall is on the scale of micrometres [14,30]. Thus, although the pumping efficiency in our models is meant to estimate the efficiency *in vivo*, the volume flow rates are not.

Though following the same trend, the hoop-stress model and the 3D simulations differ noticeably in terms of pumping efficiency (figure 6f,i). In the hoop-stress model, the flow resistance of the gaps is proportional to Tg^3, according to equation (2.9), which is based on the realistic slit shape of the gaps [10]. Yet in the 3D simulation, where the gaps are modelled as square or rectangular holes, the flow resistance is proportional to Tg^4, according to the solution of Stokes flow passing through a tube of rectangular cross section [9]. Therefore, the flow resistance for the 3D simulation is more sensitive to the value of the gap width g. The pumping efficiency calculated from 3D simulations is always higher than that predicted by the hoop-stress model. Choosing extreme aspect ratios of the gap to match the realistic geometry for the 3D simulation introduces extra deformation, as discussed in §3 (figure 6i). Therefore, we do not expect the 3D simulation to exactly match the hoop-stress model.

Our model is built on the assumption that astrocyte endfeet surrounding penetrating PVSs are separated by gaps which can expand and contract. At least one prior model [4] made the same assumption. Those gaps are known to lack the tight junctions that connect vascular endothelial cells [31], suggesting they could expand and contract. Gap width has been estimated to be as small as 20 nm [15] or as large as 5.1 μm [32]. If the gaps are prevented from expanding and contracting by some mechanical constraint, such as gap junctions that bind adjacent endfeet to each other or proteins spanning between endfeet, no such valve action would occur. On the other hand, if expansion and contraction do occur, and alter proteins on or near the endfeet, further biochemical processes might ensue. We leave the exploration of such processes for future work.

Finally, we point out that the valve mechanism proposed here, like those in other recent studies [4,5], includes and depends on a net flow of CSF out of an arterial PVS into the ECS through endfoot gaps, and hence it has a direct bearing on the important unresolved question of whether solute transport in the interstitium is due to a combination of advection and diffusion, or to diffusion alone. The glymphatic model includes a slow flow of ISF that transports solutes in the ECS in the parenchyma [33], but detecting such a flow directly poses a significant challenge (see the recent reviews [2,3]). An early study [34] found evidence of parenchymal flow in white matter but not in grey matter. Another study [35] found a dependence of solute transport on particle size and concluded that transport in the parenchyma is by diffusion alone: however, the basis of this finding has been questioned

[28]. More recent studies have provided indirect experimental evidence for flow of ISF in the parenchyma [36–38]: these studies present models that show a better fit to tracer data when such a flow is included than when it is not. There is also a theoretical argument for parenchymal flow [18] based on the observed wake/sleep variation in solute clearance [7]. An inherent feature of the endfoot valve mechanism we present here is a net flow of CSF into the interstitium, which would act as a source of new ISF. This net flow, if it occurs, would also necessarily drive a slow flow of ISF within the interstitium, but predicting the speed and distribution of this flow would require a more comprehensive and complicated model than the local model presented here.

References

1. Thomas JH. 2019 Fluid dynamics of cerebrospinal fluid flow in perivascular spaces. J. R. Soc. Interface 16, 52–57. (doi:10.1098/rsif.2019.0572)

2. Bohr T et al. 2022 The glymphatic system: current understanding and modeling. iScience 25, 104987. (doi:10.1016/j.isci.2022.104987)

3. Kelley DH, Thomas JH. 2023 Cerebrospinal fluid flow. Annu. Rev. Fluid Mech. 55, 237–264. (doi:10.1146/annurev-fluid-120720-011638)

4. Bork PAR, Ladrón-de Guevara A, Christensen AH, Jensen KH, Nedergaard M, Bohr T. 2023 Astrocyte endfeet may theoretically act as valves to convert pressure oscillations to glymphatic flow. J. R. Soc. Interface 20, 20230050. (doi:10.1098/rsif.2023.0050)

5. Gan Y, Holstein-Rønsbo S, Nedergaard M, Boster KA, Thomas JH, Kelley DH. 2023 Perivascular pumping of cerebrospinal fluid in the brain with a valve mechanism. J. R. Soc. Interface 20, 20230288. (doi:10.1098/rsif.2023.0288)

6. Roylance D 2001 Pressure vessels. Cambridge, MA: Department of Materials Science and Engineering, MIT.

7. Xie L et al. 2013 Sleep drives metabolite clearance from the adult brain. Science 342, 373–377. (doi:10.1126/science.1241224)

8. Holstein-Rønsbo S et al. 2023 Glymphatic influx and clearance are accelerated by neurovascular coupling. Nat. Neurosci. 26, 1042–1053. (doi:10.1038/s41593-023-01327-2)

9. White FM. 2006 Viscous fluid flow, 3rd edn. New York, NY: McGraw-Hill.

10. Tithof J, Boster KA, Bork PA, Nedergaard M, Thomas JH, Kelley DH. 2022 A network model of glymphatic flow under different experimentally-motivated parametric scenarios. iScience 25, 104258. (doi:10.1016/j.isci.2022.104258)

11. de Guevara AL, Shang JK, Nedergaard M, Kelley DH. 2022 Perivascular pumping in the mouse brain: improved boundary conditions reconcile theory, simulation, and experiment. J. Theor. Biol. 542, 111103. (doi:10.1016/j.jtbi.2022.111103)

12. Kedarasetti RT, Turner KL, Echagarruga C, Gluckman BJ, Drew PJ, Costanzo F. 2020 Functional hyperemia drives fluid exchange in the paravascular space. Fluids Barriers CNS 17, 52. (doi:10.1186/s12987-020-00214-3)

13. Bojarskaite L, Vallet A, Bjørnstad DM, Gullestad Binder KM, Cunen C, Heuser K, Kuchta M, Mardal KA, Enger R. 2023 Sleep cycle-dependent vascular dynamics in male mice and the predicted effects on perivascular cerebrospinal fluid flow and solute transport. Nat. Commun. 14, 953. (doi:10.1038/s41467-023-36643-5)

14. Koch T, Vinje V, Mardal KA. 2023 Estimates of the permeability of extra-cellular pathways through the astrocyte endfoot sheath. Fluids Barriers CNS 20, 20. (doi:10.1186/s12987-023-00421-8)

15. Mathiisen TM, Lehre KP, Danbolt NC, Ottersen OP. 2010 The perivascular astroglial sheath provides a complete covering of the brain microvessels: an electron microscopic 3D reconstruction. Glia 58, 1094–1103. (doi:10.1002/glia.20990)

16. Mestre H et al. 2018 Flow of cerebrospinal fluid is driven by arterial pulsations and is reduced in hypertension. Nat. Commun. 9, 4878. (doi:10.1038/s41467-018-07318-3)

17. Nicholson C, Hrabětová S. 2017 Brain extracellular space: the final frontier of neuroscience. Biophys. J. 113, 2133–2142. (doi:10.1016/j.bpj.2017.06.052)

18. Thomas JH. 2022 Theoretical analysis of wake/sleep changes in brain solute transport suggests a flow of interstitial fluid. Fluids Barriers CNS 19, 30. (doi:10.1186/s12987-022-00325-z)

19. Holter KE et al. 2017 Interstitial solute transport in 3D reconstructed neuropil occurs by diffusion rather than bulk flow. Proc. Natl Acad. Sci. USA 114, 9894–9899. (doi:10.1073/pnas.1706942114)

20. Basser PJ. 1992 Interstitial pressure, volume, and flow during infusion into brain tissue. Microvasc. Res. 44, 143–165. (doi:10.1016/0026-2862(92)90077-3)

21. Chourdakis G et al. 2022 preCICE v2: a sustainable and user-friendly coupling library [version 2; peer review: 2 approved]. Open Res. Eur. 2, 51. (doi:10.12688/openreseurope.14445.2)

22. Weller HG, Tabor G, Jasak H, Fureby C. 1998 A tensorial approach to computational continuum mechanics using object-oriented techniques. Comput. Phys. 12, 620–631. (doi:10.1063/1.168744)

23. Scroggs MW, Dokken JS, Richardson CN, Wells GN. 2022 Construction of arbitrary order finite element degree-of-freedom maps on polygonal and polyhedral cell meshes. ACM Trans. Math. Softw. 48, 18:1–18:23. (doi:10.1145/3524456)

24. Scroggs MW, Baratta IA, Richardson CN, Wells GN. 2022 Basix: a runtime finite element basis evaluation library. J. Open Sourc. Softw. 7, 3982. (doi:10.21105/joss.03982)

25. Alnaes MS et al. 2015 The FEniCS project version 1.5. Arch. Numer. Softw. 3, 100. (doi:10.11588/ans.2015.100.20553)

26. Aldea R, Weller RO, Wilcock DM, Carare RO, Richardson G. 2019 Cerebrovascular smooth muscle cells as the drivers of intramural periarterial drainage of the brain. Front. Aging Neurosci. 11, 11:1. (doi:10.3389/fnagi.2019.00001)

27. Markert B. 2005 Porous media viscoelasticity with application to polymeric foams. PhD dissertation, University of Stuttgart, Germany.

28. Mestre H et al. 2018 Aquaporin-4-dependent glymphatic solute transport in the rodent brain. eLife 7, e40070. (doi:10.7554/eLife.40070)

29. Romanò F, Suresh V, Galie PA, Grotberg JB. 2020 Peristaltic flow in the glymphatic system. Sci. Rep. 10, 21065. (doi:10.1038/s41598-020-77787-4)

30. Wang MX, Ray L, Tanaka KF, Iliff JJ, Heys J. 2021 Varying perivascular astroglial endfoot dimensions along the vascular tree maintain perivascular-interstitial flux through the cortical mantle. *Glia* **69**, 715–728. (doi:10.1002/glia.23923)

31. Plog BA, Nedergaard M. 2018 The glymphatic system in central nervous system health and disease: past, present, and future. *Annu. Rev. Pathol.-Mech.* **13**, 379–394. (doi:10.1146/annurev-pathol-051217-111018)

32. Korogod N, Petersen CC, Knott GW. 2015 Ultrastructural analysis of adult mouse neocortex comparing aldehyde perfusion with cryo fixation. *eLife* **4**, e05793. (doi:10.7554/eLife.05793)

33. Iliff J *et al.* 2012 A paravascular pathway facilitates CSF flow through the brain parenchyma and the clearance of interstitial solutes, including amyloid β. *Sci. Transl. Med.* **4**, 147ra111. (doi:10.1126/scitranslmed.3003748)

34. Rosenberg GA, Kyner WT, Estrada E. 1980 Bulk flow of brain interstitial fluid under normal and hyperosmolar conditions. *Am. J. Physiol.* **238**, F42–F49. (doi:10.1152/ajprenal.1980.238.1.F42)

35. Smith AJ, Yao X, Dix JA, Jin BJ, Verkman AS. 2017 Test of the 'glymphatic' hypothesis demonstrates diffusive and aquaporin-4-independent solute transport in rodent brain parenchyma. *eLife* **6**, e27679. (doi:10.7554/eLife.27679)

36. Ray LA, Iliff JJ, Heys JJ. 2019 Analysis of convective and diffusive transport in the brain interstitium. *Fluids Barriers CNS* **16**, 6. (doi:10.1186/s12987-019-0126-9)

37. Koundal S *et al.* 2020 Optimal mass transport with Lagrangian workflow reveals advective and diffusion driven solute transport in the glymphatic system. *Sci. Rep.* **10**, 1990. (doi:10.1038/s41598-020-59045-9)

38. Vinje V, Zapf B, Ringstad G, Eide PK, Rognes ME, Mardal KA. 2023 Human brain solute transport quantified by glymphatic MRI-informed biophysics during sleep and sleep deprivation. *Fluids Barriers CNS* **20**, 62. (doi:10.1186/s12987-023-00459-8)

39. Gan Y. 2023 Gaps in the wall of a perivascular space act as valves to produce a directed flow of cerebrospinal fluid: a hoop-stress model. Zenodo. (https://zenodo.org/records/10732126)

40. Squillacote AH, Ahrens J, Law C, Geveci B, Moreland K, King B. 2007 *The Paraview guide*, vol. 366. New York, NY: Kitware Clifton Park.